Modification of the van der Waals interaction at the Bi_2Te_3 and Ge(111) interface

Kenji Nawa,[1,2] Demie Kepaptsoglou,[3,4,†] Arsham Ghasemi,[3] Philip Hasnip,[3] Guillermo Bárcena-González,[5] Giuseppe Nicotra,[6] Pedro L. Galindo,[5] Quentin M. Ramasse,[4,7] Kohji Nakamura,[2] Susannah C. Speller[8], Balati Kuerbanjiang,[9] Thorsten Hesjedal,[9†] and Vlado K. Lazarov[3†]

[1]Research Center for Magnetic and Spintronic Materials, National Institute for Materials Science (NIMS), 1-2-1 Sengen, Tsukuba, Ibaraki 305-0047, Japan

[2]Department of Physics Engineering, Mie University, 1577 Kurima-machiya, Tsu, Mie 514-8507, Japan

[3]Department of Physics, University of York, York YO10 5DD, United Kingdom

[4]SuperSTEM Laboratory, SciTech Daresbury Campus, Daresbury WA4 4AD, United Kingdom

[5]Department of Computer Engineering, ESI, University of Cádiz, 11510, Puerto Real, Spain

[6]CNR-IMM, Strada VIII, 5, 95121 Catania, Italy

[7]School of Chemical and Process Engineering and School of Physics and Astronomy, University of Leeds, Leeds LS2 9JT, UK

[8] Department of Materials, University of Oxford, Oxford, OX1 3PH, United Kingdom

[9]Department of Physics, Clarendon Laboratory, University of Oxford, Oxford OX1 3PU, United Kingdom

[†] Authors to whom correspondence should be addressed: dmkepap@superstem.org, vlado.lazarov@york.ac.uk, and Thorsten.Hesjedal@physics.ox.ac.uk

ABSTRACT

We present a structural and density functional theory study of the interface of the quasi-twin-free-grown three-dimensional topological insulator Bi_2Te_3 on Ge(111). Aberration-corrected scanning transmission electron microscopy and electron energy-loss spectroscopy in combination with first-principles calculations show that the weak van der Waals adhesion between the Bi_2Te_3 quintuple layer and Ge can be overcome by forming an additional Te layer at their interface. The first-principles calculations of the formation energy of the additional Te layer show it to be energetically favorable as a result of the strong hybridization between the Te and Ge.

I. INTRODUCTION

Bi_2Se_3, Bi_2Te_3, and Sb_2Te_3 are three-dimensional topological insulators (TIs) [1,2] that have been attracting great attention in recent years due to their topologically protected, fully spin-polarized surfaces states. These spin-momentum-locked surface states, protected by time reversal symmetry, have been the focus of numerous studies owing to their potential spintronics application [3–7]. In addition, a variety of interesting physical phenomena have been observed and are predicted to occur in these materials, including the quantum anomalous Hall effect, [8] the topological magneto-electric effect, [9] image magnetic monopoles, [10] and Majorana fermions. [11]

The incorporation of TIs in device structures requires the fabrication of these materials as thin films. Thin film TIs have already been successfully used in spintronics applications, e.g., based on spin accumulation and spin-transfer torque. [7,12] High-quality, single-crystalline films are usually grown by molecular beam epitaxy (MBE). Consequently, MBE growth studies of Bi_2Se_3 and Bi_2Te_3 thin films have been carried out on a variety of substrates, e.g., Si(001) and (111), [13] GaN(001), [14] GaAs(001) and (111), [12,15] CdTe(111), [16] SiC(001), [17] as well as on lattice-matched InP(111) [18] and, more recently, Bi_2Se_3 was grown on Ge(111). [19,20] From a technological point of view, the integration of TIs with long-spin-diffusion-length semiconductor materials such as germanium seems to be a very promising solution for the current CMOS (complementary metal-oxide-semiconductor) technology limitations. [21]

One of the challenges for monolithic device integration of TIs is their weak bonding to most substrates, originating from the van der Waals (vdW)-type interaction between film and substrate. While vdW bonding (inherent to the layered nature of the $(Sb,Bi)_2(Se,Te)_3$ TI family) can be exploited for overcoming the lattice mismatch in TI-based heterostructures, [22] the

weak bonding between TI film and substrate can significantly increase the density of domain boundaries [16] and the formation of rotational twins. As expected, twin formation can be suppressed by growing on perfectly lattice-matched substrates like the insulating BaF_2(111). [23]

In this work we show that the Bi_2Te_3 bonding strength to a Ge(111) substrate is significantly increased by the atomic structure changing at the interface. In particular, the formation of an interfacial inverted Ge-Te dumbbell layer, formed between the Bi_2Te_3 film and the Ge(111) substrate overcomes the inherently weak bonding between the Te-terminated Te-Bi-Te-Bi-Te quintuple layers (QLs) and Ge. The stability of this interfacial layer was confirmed by density functional theory (DFT) calculations, which also show that the Te-Ge dumbbell enables atomic hybridization with the layers in proximity to the interface.

II. EXPERIMENTAL

The Bi_2Te_3 thin films were grown in a Createc MBE system with a base pressure of 1×10^{-10} Torr. Bi and Te (99.9999% pure elemental source material) were co-evaporated out of standard effusion cells with a Te:Bi flux ratio of 10:1, as calibrated using an *in-situ* beam flux monitor. This overpressure of the chalcogenide has been shown to be necessary to reduce the Te vacancy defects in the film. The Ge wafers were degreased in solvents, rinsed in de-ionized water, and then baked in vacuum to 250°C for 8 hours to leave a clean surface for growth. As-prepared Ge substrates have a surface oxide layer which is easily desorbed by heating to higher (~600°C) substrate temperatures. The temperature is measured by a thermocouple which is fixed right under the substrate holder during growth, and the surface evolution is checked by RHEED. The deposition rate of the Bi_2Te_3 films was typically ~0.5 nm/min. The Bi_2Te_3 films were grown in a two-step growth process. First, a 3-nm-thick

nucleation layer was deposited at a lower temperature of 200 °C. Subsequently, this layer was annealed at 300 °C for 30 minutes (with the Bi shutter closed), before continuing the growth at 300 °C up to the desired film thickness. The film quality was evaluated using *in-situ* reflection high-energy electron diffraction (RHEED) and *ex-situ* X-ray diffraction (XRD).

Cross-sectional transmission electron microscopy (TEM) specimen preparation was carried out by focused ion beam milling using a FEI Helios NanoLab 600 instrument.[23] Scanning transmission electron microscopy (STEM) imaging and electron energy-loss spectroscopy (EELS) measurements were performed in a Nion UltraSTEM100 equipped with a Gatan Enfina spectrometer. The microscope was operated at 100 kV, with a beam convergence angle of 31 mrad, resulting in an electron probe size of ~0.8 Å. The inner and outer detector angles for high angle annular dark field (HAADF)-STEM imaging was 76-200 mrad. The EELS collection angle was 33 mrad. Additional atomic-resolution imaging was carried out using a JEOL ARM200F probe-corrected (S)TEM instrument, operated at 200 kV acceleration voltage and the probe-forming optics were configured to form a ~0.8 Å probe. The semi-angular range of the HAADF detector was 72-200 mrad. In order to reduce noise in the EELS data, principal component analysis was applied using Hyperspy [24]. The images used for the estimation of the interatomic distances were obtained by rapidly acquiring series (or 'stacks') of consecutive images, subsequently averaged into a single image using rigid and non-rigid reconstruction techniques, as implemented in the SmartAlign plugin for Digital Micrograph [25] ; scanning distortions in the images were corrected using the Jitterbug [26] plugin for Digital Micrograph. This approach can provide near picometer precision in distance determination. [27] The reconstructed images were further checked for calibration using the interatomic distances of the Ge [112] dumbbell distance (~0.082nm) as an internal, self-consistent reference, which are clearly resolved in the images. The strain at the interface was analysed using geometric phase analysis (GPA) of STEM images. [28] GPA strain measures

were obtained after using a substrate as a reference. The axes were chosen along the principal directions of elastic symmetry, taking the x-axis parallel to the interface and the y-axis normal to the interface.

DFT calculations were performed to investigate the stability of the interfacial atomic structure. The calculations were carried out by the all-electron, full-potential linearized augmented plane wave (FLAPW) method with a single slab geometry. [29–31] The LAPW basis functions are expanded within a cut-off of $|k + G| \leq 3.9$ a.u.$^{-1}$ and muffin-tin (MT) sphere radii of 2.7, 2.5, and 2.1 bohr were used for Bi, Te, and Ge atoms, respectively. The angular momentum expansions inside the MT spheres were truncated at ℓ=8 for the wave functions, charge density, and potential. The generalized gradient approximation [29] was used for the exchange-correlation functional. We considered in total four models: model-1 is the reference Bi_2Te_3/Ge system, model-2 has a monolayer of Te between substrate and the first QL: Bi_2Te_3/Te/Ge_{sub}, model-3 with Bi_2Te_3/**Ge/Te**/Ge_{sub}, and model-4 with Bi_2Te_3/**Te/Ge**/Ge_{sub} representing the modification of the dumbbell structure of Ge with Te. For model-1 and -2, three QLs of Bi_2Te_3 and 12 atomic layers of Ge were used as representation of the film and the Ge(111) substrate, while for model-3 and -4, 11 atomic layers of Ge and a monolayer of Te were chosen as the dumbbell-stacked structure. All four models are presented in the supplementary material in **Fig. S1.** [32] The in-plane lattice constant of the supercells used for the calculations was fixed to that of bulk Bi_2Te_3, 4.386 Å. Interfacial distances were theoretically determined by including the vdW interaction by semi-empirical dispersion-corrected DFT-D3 calculations [31]; the fcc-like atomic stacking was found to be stable in all considered model interfaces. Atoms in the bottom three Ge layers are fixed to the bulk geometry, while all other atoms were fully relaxed by the force calculations. The Brillouin zone (BZ) was sampled with a 41×41 ***k***-point mesh in the 2D BZ.

III. RESULTS AND DISCUSSION

Figs. 1(a) and 1(b) show the RHEED patterns of the Ge substrate and the Bi_2Te_3 film, respectively. We note that the Ge(111) surface, based on the RHEED pattern (Fig. 1a), shows the typical c (2×8) surface reconstruction, [21] which is the result of substrate annealing at 600°C for 30 mins. The sharp streaks indicate a flat surface for both the Ge(111) substrate and the grown Bi_2Te_3 film. The difference in the RHEED patterns, *i.e.*, the presence of spots in the RHEED streaks from the substrate in comparison to the film, indicates the presence of terrace steps on the substrate, as also evident from HAADF-STEM imaging (see also Fig. S2 in the supplementary material [32]). The structural order of the films was examined by X-ray diffraction (XRD). Fig. 1(c) shows that the films are single-crystalline and free from secondary phases. The peaks labelled (00*l*) are consistent with the $R\bar{3}m$ space group of the *c*-axis oriented (growth direction along [001]) rhombohedral Bi_2Te_3 film. The *c*-axis lattice constant is found to be (30.47 ± 0.01) Å, which is comparable to the value of 30.48 Å obtained for Bi_2Te_3 bulk crystals.

In order to investigate the structural ordering of the Bi_2Te_3 film and Ge/Bi_2Te_3 interface at the atomic scale, we performed atomic-resolution STEM imaging and EELS spectroscopy. A HAADF-STEM overview image of the Bi_2Te_3 film on the Ge substrate is shown in Fig. 2(a), confirming the overall uniform film growth. Fig. 2(b) gives a closer view of the interfacial region between Ge and Bi_2Te_3; the atomically resolved HAADF image shows clearly the continuous QL structure of the Bi_2Te_3 film, and the distinct crystallographic discontinuity between the Ge substrate and the film. A closer observation of the interface (between the Ge dumbbell and first QL layer) shows the presence of a bright contrast region, with a size commensurate to that of an atomic monolayer parallel to the Ge substrate (marked by a red arrow in Fig. 2(b)), followed by an area of a darker contrast before the first Bi_2Te_3 QL layer, indicating the formation of an interfacial layer. A close-up view of the interface is shown in

Fig. 2(c), where the atomic structure of the QL of Bi_2Te_3 along the [11$\bar{2}$0] zone axis is clearly resolved, with heavier Bi (Z_{Bi}=83) atomic columns (marked with blue circles in Fig. 2(c)) being clearly brighter compared to Te (Z_{Te}=52) columns (marked with red circles in Fig. 2(c)). Similarly, the dumbbell structure of Ge along the [11$\bar{2}$] zone axis can be clearly observed (marked with green circles in Fig. 2(c)). We note that after the first QL layer, the films appear in the projection as septuple layers. This could be due to slightly off-stoichiometric film growth indicated by the shoulder on the (006) and (0015) XRD peaks, or it could be due to the existence of film grains that are nucleated on different surface steps. For cross-sectional imaging, the overlapping of grains would also shift the QL layers, and in projection, they can appear as a septuple layers. [17]

A closer inspection of the interface region confirms the presence of an interface layer, which appears to comprise a continuous bright atomic monolayer (denoted as ML1 in Fig. 2(c)) of brighter contrast at the Ge substrate side (marked by a red arrow in Fig. 2(c)), followed by an atomic monolayer (ML2) of relatively lower intensity before the first Bi_2Te_3 QL (marked by a green arrow in Fig. 2(c)). The distances of ML1 from the terminating Ge1 atom and first Te1 atom of the QL layer were determined to be ~2.92 and ~3.68 Å, respectively. The corresponding distances for ML2 were ~4.32 and ~2.28 Å, respectively (see also supplementary Fig. S3 [32]). The distance between ML1 and ML2 was determined to be ~1.48 Å (the error in distance determination is estimated to be ±0.18 Å, determined from the standard deviation of the Ge [112] dumbbell distance). It should be noted, that in the HAADF image of Fig. 2(c) ML2 appears somewhat interrupted, possibly due to surface damage of the specimen at thinner areas of the sample. Additional imaging from thicker, less damaged areas of the specimen (see also supplementary Fig. S4 [32]), confirm the observation of a continuous ML2 of lower intensity. The relative image intensity clearly points to a distinct difference in the chemistry of the two MLs; the brighter ML1 is a heavier element, possibly Te or Bi, while

the intensity of the darker ML2 is closer to that of the Ge substrate. It is however, difficult to determine the interfacial layer chemistry from imaging alone.

For this we turn to chemical analysis at atomic resolution by STEM-EELS measurements, during which the electron probe is rastered across a defined region and an EEL spectrum is acquired at each point, simultaneously with the corresponding HAADF intensity [33]. Fig. 3 shows an example of such a measurement; Fig. 3(a) is the HAADF-STEM survey image in which the region selected for the EELS measurements is outlined by a yellow box. The maps of the Te $M_{4,5}$ and Ge $L_{2,3}$ ionization edge signals shown in Figs. 3(c) and 3(d), respectively, are produced by integrating the signal above the relevant ionisation edge onset over a 100 eV window, after subtraction of the decaying background using a power-law model. Comparing the simultaneously acquired HAADF signal (Fig. 3(b)) with the Te and Ge elemental maps (Figs. 3(c) and 3(d), respectively, also plotted as line profiles in Fig. 3(f)), suggests that ML1 consists predominantly of Te, consistent with the higher image intensity next to the last Ge dumbbells (for reading clarity the maps have been overlaid in Fig 3(e)). The Ge signal initially extends with decaying intensity into the film, but the intensity increases locally at the position of ML2, also consistent with the observed lower intensity before the first Bi_2Te_3 QL layer. This unexpected observation implies that the structure of the interfacial layer at the Bi_2Te_3/Ge interface is that of an inverted Ge-Te dumbbell-like structure (QL_{Bi2Te3}/**Ge/Te/** Ge_{sub}). It is interesting to note that experimental surface studies on Te monolayers on Ge(100) show the unusual formation of Te-Ge dimers, [34]which may also occur on the Ge(111) surface, thus providing the mechanism for inverted dumbbell formation. However, further studies are necessary to shed light on the mechanisms that drive the formation of the observed interface structure in our films.

It should be pointed out that because of the presence of interfacial terraces (Fig. S2), the possibility that the observation of the inverted Ge-Te dumbbell could arise as a result of a

geometric projection effect (from QL layers grown on terraces with steps of one Ge-dumbbell) cannot be entirely excluded, although from extensive imaging of equivalent regions of the sample of varying thickness it is considered unlikely.

In order to understand how the electronic structure of the interface is modified by the presence of the interfacial layer(s), we conducted comprehensive DFT calculations. We considered in total four models, Fig. S1 of the supplementary material. [32] Model-1 is the reference Bi_2Te_3/Ge system and model-2 has only a single layer of Te between the QL and the substrate: QL_{Bi2Te3}/**Te**/Ge_{sub}. Model-3 with QL_{Bi2Te3}/**Te/Ge**/Ge_{sub}, and model-4 with QL_{Bi2Te3}/**Ge/Te/** Ge_{sub} include interfacial dumbbell interface layers, with both a Ge-Te termination (model-3) and an inverted Te-Ge dumbbell structure (model-4). For the model-1 and -2, three QLs of Bi_2Te_3 and 12 atomic layers of Ge were used as representation of the film and the Ge(111) substrate, while for model-3 and -4, 11 atomic layers of Ge and a monolayer of Te as the dumbbell-stacked structure were considered. In order to discuss the energetics of these systems, we have calculated the formation energy, E_{Form}, by the following formula:

$$E_{\mathrm{Form}} = E_{\mathrm{Total}} - \sum_i N_i \mu_i .$$

The first term is the total energy of system for all the supercell models, and for the chemical potentials the bulk values of pristine Bi_2Te_3 ($\mu_{Bi_2Te_3}$), hexagonal Te (μ_{Te}), and diamond Ge (μ_{Ge}) are taken. The coefficients N_i account for the number of QLs of Bi_2Te_3 and for the number of atoms of Te and Ge, respectively, in the simulated slab. A positive (negative) sign of E_{Form} indicates a system that is more (less) energetically stable. From the E_{Form} calculations, the largest formation-energy gain was found in model-2 with an E_{Form} difference from the reference model-1, dE_{Form} = –3.407 eV, followed by model-4 (dE_{Form} = –2.493 eV), model-3 (–2.473 eV), and model-1 (0.000 eV). The calculations show that there is a significant driving

force for the formation of an interface layer(s). However, the presence of a dumbbell-like layer suggests that other effect such as a kinetics, substrate termination, etc... also play a role of the interface layer formation. We also note that the calculated distances between layers in the relaxed structure for model-4 are in good agreement with the corresponding distances determined experimentally. Hence, the observation of the inverted dumbbell-like interface layers structure is supported by the total energy calculations of the model interfaces.

Having confirmed the energetic origin of the experimental data, *i.e.* the validity of the inverted Ge-Te dumbbell model, we explore its effect on the electronic structure at the interface. Since we are interested in the electronic structure implications of the Bi_2Te_3/dumbbell interfacial reconstruction, next we present the band structures of the last Te of the bottom QL (Te_{QL}), as well as of the Ge on top of the inverted-dumbbell and their projected densities of states (DOS), Fig. 4. The inverted dumbbell model shows that strong hybridization is taking place between Te_{QL} and Ge_{top}. This results in the bonding Te_{QL} state and antibonding Ge_{top} states around E = –2 and +2 eV, respectively. Fig. 4(d) shows the charge-density changes induced by the interface reconstruction, $\Delta n = n_{Bi_2Te_3/Ge/Te/Ge} - \left(n_{Bi_2Te_3/Ge} + n_{Ge\text{-}Te}\right)$. Significant charge density changes are found in all interface layers, at both the QL-Bi_2Te_3 and the inverted Ge-Te dumbbell layers, as well as the top dumbbell layer from Ge(111) substrate. This clearly demonstrates the role of the Ge-Te inverted-dumbbell interface layer: it significantly enhances the chemical bonding between the first Bi_2Te_3 quintuple layer and the Ge substrate.

A good insight into how interlayers change the electronic structure at the interface can be obtained by considering and comparing the interfacial electronic structure of the other models. In the reference model-1, the surface state of Ge_{top} shows a sharp peak of DOS at the Fermi level (Fig. S5(a)), which likely contributes to the high E_{Form} of this interface. The insertion of the Te_{ML} (model-2) stabilizes the interfacial electronic structure by forming an atomic orbital

hybridization between the Te_{ML} and Ge_{top} atoms, resulting in the significant change of the charge reconstruction only at the interface (Fig. S5(b)). Introducing dumbbell layers further modifies the electronic structure; we note that the Te-Ge dumbbell interface (model-3) shows almost no direct hybridization between Te_{QL} and Te_{ML} of the Te-Ge dumbbell due to the rather long interface distance, 4.97 Å (Fig. S5(c)). A further gain in energy is obtained by the inverted dumbbell structure, which provides the strongest bonding across the interface, as discussed above.

The strong chemical bonding enabled by the Te_{ML} layer at the interface is also evident in the epitaxy between the film and the substrate. While the van der Waals interfacial bonding allows for significant strain accommodation at the interfaces [18,35–37], without the need for keeping the registry of atomic stacking at the interface, the strong bonding across heterointerfaces even for a small lattice mismatch (<1%) induces the formation of a dislocation network through which the strain energy at the interface is minimized. Hence, the formation of a dislocation network is expected to occur for the Bi_2Te_3/Ge when the van der Waals bonding is suppressed. Fig. S6 in the supplementary material, [32] indeed shows clearly the presence of interface dislocations at the Bi_2Te_3/Te/Ge/Ge_{sub} interface, that appear at nearly periodic distances of ~10 atomic planes, reflecting the 10 % mismatch between film and substrate. The strain caused by the formation of the misfit dislocations is shown in Fig.5. Finally, we note that a strong bonding between the film and substrate also suppresses the formation of rotational twin grains as evidenced by the electron backscatter diffraction (EBSD) patterns from the grown films (Fig. S7).

IV. SUMMARY

In summary, we have demonstrated the modified van der Waals epitaxy MBE growth of Bi_2Te_3 on Ge(111). Using aberration corrected STEM and EELS, we found that an inverted Ge-Te

dumbbell layer has formed at the interface of Bi_2Te_3 and Ge(111), which drastically changes the electronic structure and bonding across the interface. DFT total energy calculations reveal that the formation of the inverted Ge-Te dumbbell layer is favorable compared to Te-Ge. Electronic band structure calculations reveal that the stronger atomic *p*-type orbital hybridization at the interface overcomes the inherent weak bonding between Bi_2Te_3 and Ge. Finally, our results demonstrate that in contrast to other Bi_2Te_3-substrate systems, which are governed by van der Waals epitaxy, the growth on Ge(111), due to the formation of the Te-Ge inverted dumbbell, is governed by an intimate interaction between film and substrate. Our work illustrates that weak bonding in topological insulator heterostructures can be overcome by suitable atomic interface engineering, which is of great importance for fabricating monolithic device structures with full control of the epitaxial relationship.

ACKNOWLEDGMENTS

This publication arises from research funded by the John Fell Oxford University Press (OUP) Research Fund. The authors thank L. J. Collins-McIntyre for help with the initial sample preparation and analysis. Diamond Light Source is thanked for access to the Surfaces and Interfaces Laboratory facilities. The SuperSTEM Laboratory is the UK National Research Facility for Advanced Electron Microscopy, supported by the Engineering and Physical Sciences Research Council (EPSRC). V.K.L., T.H., and B.K. acknowledge financial support from the Engineering and Physical Sciences Research Council (UK) through Grants EP/K03278X/1 and EP/N032128/1. Part of this work was performed at Beyondnano CNR-IMM, which is supported by the Italian Ministry of Education and Research (MIUR) under project Beyond – Nano (PON a3_00363).

K.N. is grateful to M. Weinert at the University of Wisconsin-Milwaukee for critical comments and to Y. Miura and S. Mitani at NIMS for fruitful discussions. K.N. also acknowledges financial support from the Japan Public-Private Partnership Student Study Abroad Program "TOBITATE Young Ambassador Program" by MEXT. Work at Mie University was supported by JSPS KAKENHI Grant Numbers JP15H05702 and JP16J07422, and the Research Programs for Next Generation Young Scientists of "Five-star Alliance" in "NJRC Mater. & Dev." Grants No. 20175023. Computations were performed by the facilities of the Supercomputer Center, the Institute for Solid State Physics, the University of Tokyo, and by Numerical Materials Simulator at NIMS.

We declare no conflicts of interests.

REFERENCES

[1] X.-L. Qi and S.-C. Zhang, *The Quantum Spin Hall Effect and Topological Insulators*, Phys. Today **63**, 33 (2010).

[2] M. Z. Hasan and C. L. Kane, *Colloquium: Topological Insulators*, Rev. Mod. Phys. **82**, 3045 (2010).

[3] H. Zhang, C.-X. Liu, X.-L. Qi, X. Dai, Z. Fang, and S.-C. Zhang, *Topological Insulators in Bi2Se3, Bi2Te3 and Sb2Te3 with a Single Dirac Cone on the Surface*, Nat. Phys. **5**, 438 (2009).

[4] Y. Xia, D. Qian, D. Hsieh, L. Wray, A. Pal, H. Lin, A. Bansil, D. Grauer, Y. S. Hor, and R. J. Cava, *Observation of a Large-Gap Topological-Insulator Class with a Single Dirac Cone on the Surface*, Nat. Phys. **5**, 398 (2009).

[5] D. Hsieh, Y. Xia, D. Qian, L. Wray, F. Meier, J. H. Dil, J. Osterwalder, L. Patthey, A. V Fedorov, H. Lin, A. Bansil, D. Grauer, Y. S. Hor, R. J. Cava, and M. Z. Hasan, *Observation of Time-Reversal-Protected Single-Dirac-Cone Topological-Insulator States in Bi_2Te_3 and Sb_2* , Phys. Rev. Lett. **103**, 146401 (2009).

[6] Y. L. Chen, J. G. Analytis, J.-H. Chu, Z. K. Liu, S.-K. Mo, X. L. Qi, H. J. Zhang, D. H. Lu, X. Dai, Z. Fang, S. C. Zhang, I. R. Fisher, Z. Hussain, and Z.-X. Shen, *Experimental Realization of a Three-Dimensional Topological Insulator, Bi_2Te_3*, Science **325**, 178 (2009).

[7] A. R. Mellnik, J. S. Lee, A. Richardella, J. L. Grab, P. J. Mintun, M. H. Fischer, A. Vaezi, A. Manchon, E.-A. Kim, N. Samarth, and D. C. Ralph, *Spin-Transfer Torque Generated by a Topological Insulator*, Nature **511**, 449 (2014).

[8] C.-Z. Chang, J. Zhang, X. Feng, J. Shen, Z. Zhang, M. Guo, K. Li, Y. Ou, P. Wei, L.-L. Wang, Z.-Q. Ji, Y. Feng, S. Ji, X. Chen, J. Jia, X. Dai, Z. Fang, S.-C. Zhang, K. He, Y. Wang, L. Lu, X.-C. Ma, and Q.-K. Xue, *Experimental Observation of the Quantum Anomalous Hall Effect in a Magnetic Topological Insulator*, Science . **340**, 167 (2013).

[9] X.-L. Qi, T. L. Hughes, and S.-C. Zhang, *Topological Field Theory of Time-Reversal Invariant Insulators*, Phys. Rev. B **78**, 195424 (2008).

[10] X.-L. Qi, R. Li, J. Zang, and S.-C. Zhang, *Inducing a Magnetic Monopole with Topological Surface States*, Science (80-.). **323**, 1184 (2009).

[11] L. Fu and C. L. Kane, *Probing Neutral Majorana Fermion Edge Modes with Charge Transport*, Phys. Rev. Lett. **102**, 216403 (2009).

[12] M. Eddrief, P. Atkinson, V. Etgens, and B. Jusserand, *Low-Temperature Raman Fingerprints for Few-Quintuple Layer Topological Insulator Bi2Se3films Epitaxied on GaAs*, Nanotechnology **25**, 245701 (2014).

[13] T. Zhang, P. Cheng, X. Chen, J.-F. Jia, X. Ma, K. He, L. Wang, H. Zhang, X. Dai, Z. Fang, X. Xie, and Q.-K. Xue, *Experimental Demonstration of Topological Surface States Protected by Time-Reversal Symmetry*, Phys. Rev. Lett. **103**, 266803 (2009).

[14] M. Y. Pang, H. F. Lui, W. S. Li, K. H. Wong, and C. Surya, *Characterizations of Bismuth Telluride/Gallium Nitride Heterojunction Photovoltaic Detector for MWIR Detection under Room Temperature*, J. Phys. Conf. Ser. **152**, 12046 (2009).

[15] Z. Chen, T. A. Garcia, J. De Jesus, L. Zhao, H. Deng, J. Secor, M. Begliarbekov, L. Krusin-Elbaum, and M. C. Tamargo, *Molecular Beam Epitaxial Growth and Properties of Bi2Se3 Topological Insulator Layers on Different Substrate Surfaces*, J. Electron. Mater. **43**, 909 (2014).

[16] S. Cho, Y. Kim, A. DiVenere, G. K. Wong, J. B. Ketterson, and J. R. Meyer, *Antisite Defects of Bi2Te3 Thin Films*, Appl. Phys. Lett. **75**, 1401 (1999).

[17] Y. Liu, Y. Y. Li, S. Rajput, D. Gilks, L. Lari, P. L. Galindo, M. Weinert, V. K. Lazarov, and L. Li, *Tuning Dirac States by Strain in the Topological Insulator Bi2Se3*, Nat. Phys. **10**, 294 (2014).

[18] S. Schreyeck, N. V Tarakina, G. Karczewski, C. Schumacher, T. Borzenko, C. Brüne, H. Buhmann, C. Gould, K. Brunner, and L. W. Molenkamp, *Molecular Beam Epitaxy of High Structural Quality Bi 2 Se 3 on Lattice Matched InP(111) Substrates*, Appl. Phys. Lett. **102**, 041914 (2013).

[19] T. Guillet, C. Zucchetti, A. Marchionni, A. Hallal, P. Biagioni, C. Vergnaud, A. Marty, H. Okuno, A. Masseboeuf, M. Finazzi, F. Ciccacci, M. Chshiev, F. Bottegoni, and M. Jamet, *Spin Orbitronics at a Topological Insulator-Semiconductor Interface*, Phys. Rev. B **101**, 184406 (2020).

[20] S. Kim, S. Lee, J. Woo, and G. Lee, *Growth of Bi 2 Se 3 Topological Insulator Thin Film on Ge(1 1 1) Substrate*, Appl. Surf. Sci. **432**, 152 (2018).

[21] T. Guillet, A. Marty, C. Beigné, C. Vergnaud, M.-T. Dau, P. Noël, J. Frigerio, G. Isella, and M. Jamet, *Magnetotransport in Bi2Se3 Thin Films Epitaxially Grown on Ge(111)*, AIP Adv. **8**, 115125 (2018).

[22] A. Ghasemi, D. Kepaptsoglou, P. L. Galindo, Q. M. Ramasse, T. Hesjedal, and V. K. Lazarov, *Van Der Waals Epitaxy between the Highly Lattice Mismatched Cu-Doped FeSe and Bi2Te3*, NPG Asia Mater. **9**, e402 (2017).

[23] F. Bonell, M. G. Cuxart, K. Song, R. Robles, P. Ordejón, S. Roche, A. Mugarza, and S. O. Valenzuela, *Growth of Twin-Free and Low-Doped Topological Insulators on*

BaF 2 (111), Cryst. Growth Des. **17**, 4655 (2017).

[24] F. de la Peña, E. Prestat, V. T. Fauske, P. Burdet, P. Jokubauskas, M. Nord, T. Ostasevicius, K. E. MacArthur, M. Sarahan, D. N. Johnstone, J. Taillon, J. Lähnemann, V. Migunov, A. Eljarrat, J. Caron, T. Aarholt, S. Mazzucco, M. Walls, T. Slater, F. Winkler, pquinn-dls, B. Martineau, G. Donval, R. McLeod, E. R. Hoglund, I. Alxneit, D. Lundeby, T. Henninen, L. F. Zagonel, and A. Garmannslund, *Hyperspy/Hyperspy: HyperSpy v1.5.2*.

[25] L. Jones, H. Yang, T. J. Pennycook, M. S. J. Marshall, S. Van Aert, N. D. Browning, M. R. Castell, and P. D. Nellist, *Smart Align—a New Tool for Robust Non-Rigid Registration of Scanning Microscope Data*, Adv. Struct. Chem. Imaging **1**, 8 (2015).

[26] HREM Research, *Jitterbug for Digital Micrograph*.

[27] A. B. Yankovich, B. Berkels, W. Dahmen, P. Binev, S. I. Sanchez, S. A. Bradley, A. Li, I. Szlufarska, and P. M. Voyles, *Picometre-Precision Analysis of Scanning Transmission Electron Microscopy Images of Platinum Nanocatalysts*, Nat. Commun. **5**, 4155 (2014).

[28] P. L. Galindo, S. Kret, A. M. Sanchez, J.-Y. Laval, A. Yáñez, J. Pizarro, E. Guerrero, T. Ben, and S. I. Molina, *The Peak Pairs Algorithm for Strain Mapping from HRTEM Images*, Ultramicroscopy **107**, 1186 (2007).

[29] E. Wimmer, H. Krakauer, M. Weinert, and A. J. Freeman, *Full-Potential Self-Consistent Linearized-Augmented-Plane-Wave Method for Calculating the Electronic Structure of Molecules and Surfaces: O_2 Molecule*, Phys. Rev. B **24**, 864 (1981).

[30] M. Weinert, E. Wimmer, and A. J. Freeman, *Total-Energy All-Electron Density Functional Method for Bulk Solids and Surfaces*, Phys. Rev. B **26**, 4571 (1982).

[31] K. Nakamura, T. Ito, A. J. Freeman, L. Zhong, and J. Fernandez-de-Castro, *Enhancement of Magnetocrystalline Anisotropy in Ferromagnetic Fe Films by Intra-Atomic Noncollinear Magnetism*, Phys. Rev. B **67**, 14420 (2003).

[32] See Supplemental Material at [URL will be inserted by publisher] for additional HADDF STEM imaging data; interfacial structure models used for DFT calculations; electron backscatter diffraction (EBSD) patterns.

[33] N. D. Browning, D. J. Wallis, P. D. Nellist, and S. J. Pennycook, *EELS in the STEM: Determination of Materials Properties on the Atomic Scale*, Micron **28**, 333 (1997).

[34] P. F. Lyman, D. L. Marasco, D. A. Walko, and M. J. Bedzyk, *Multiple Bonding Configurations for Te Adsorbed on the Ge(001) Surface*, Phys. Rev. B **60**, 8704 (1999).

[35] A. Koma, *Van Der Waals Epitaxy—a New Epitaxial Growth Method for a Highly Lattice-Mismatched System*, Thin Solid Films **216**, 72 (1992).

[36] A. Koma, *Van Der Waals Epitaxy for Highly Lattice-Mismatched Systems*, J. Cryst. Growth **201**–**202**, 236 (1999).

[37] L. A. Walsh and C. L. Hinkle, *Van Der Waals Epitaxy: 2D Materials and Topological Insulators*, Appl. Mater. Today **9**, 504 (2017).

FIGURES

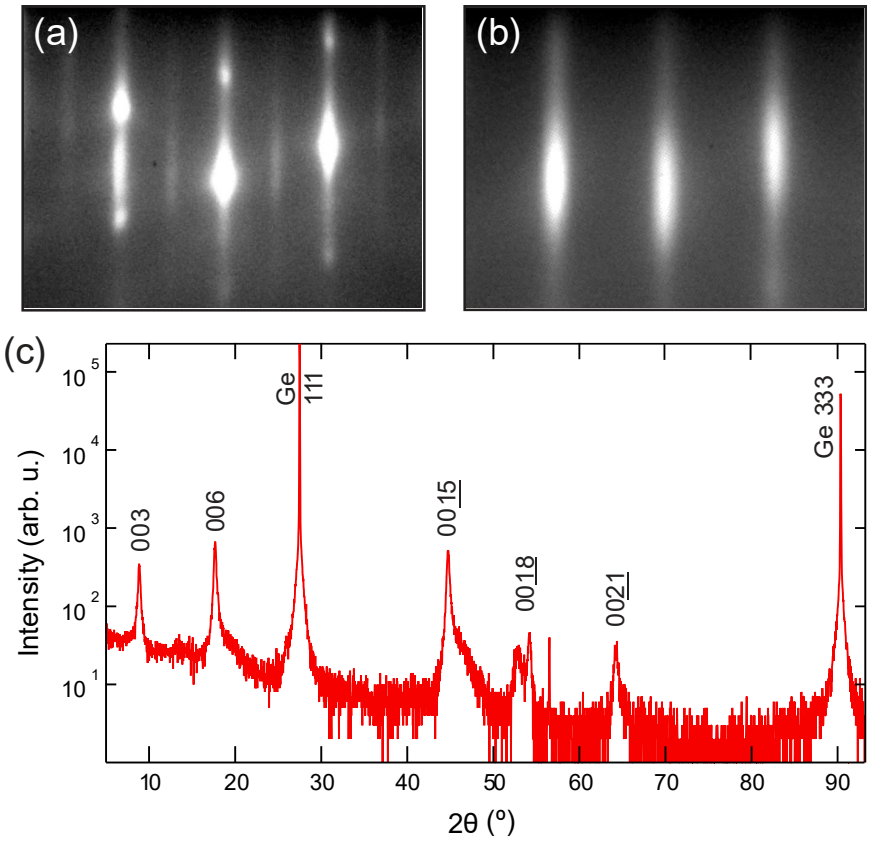

FIG. 1. (a,b) RHEED patterns obtained from the Ge and the Bi_2Te_3 surfaces, respectively. (c) X-ray diffraction spectrum showing both film and substrate peaks as labelled.

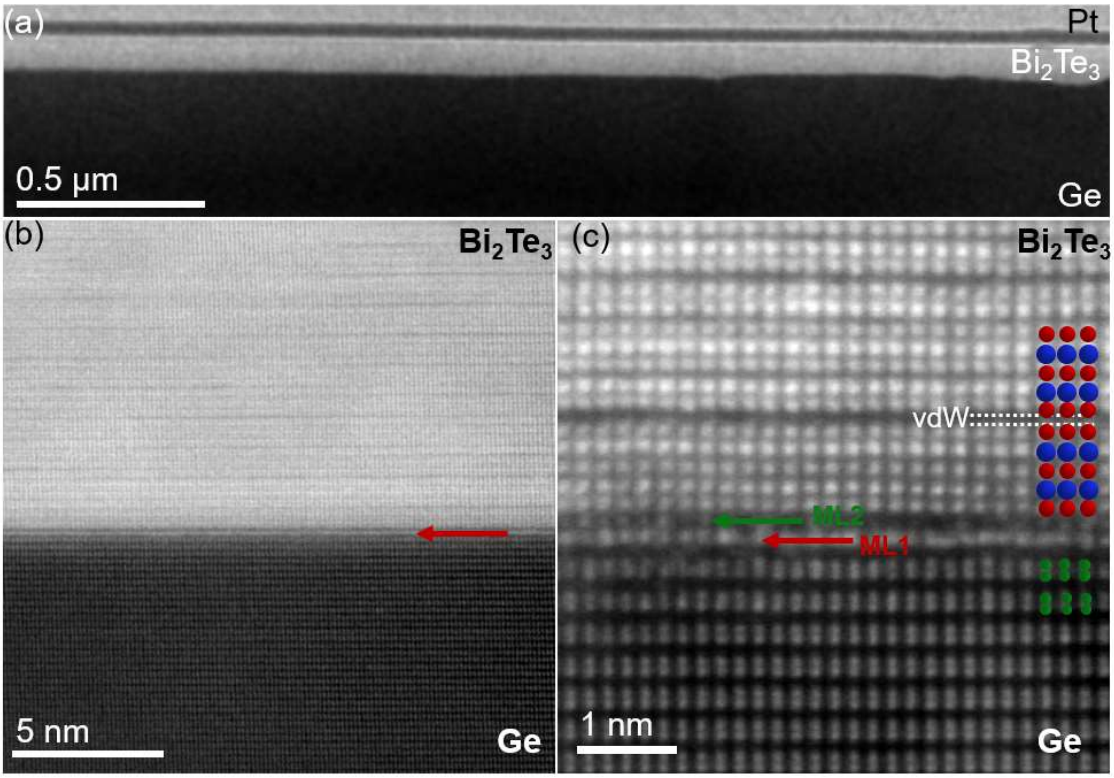

FIG. 2. (a) Overview HAADF-STEM image of the Bi_2Te_3 film on Ge(111). (b) Atomically resolved HAADF-STEM image from the interface region. (c) Detail from the interfacial region between the Bi_2Te_3 film and the Ge substrate. The overlaid structural model shows the Bi_2Te_3/Ge atomic positions as well as the extra layer at the interface; Bi (blue), Te (red), and Ge (green) atomic columns. The red arrows indicate the distinctive interface atomic MLs. A Pt layer was deposited *in-situ* for protection of the film during the FIB TEM specimen preparation process.

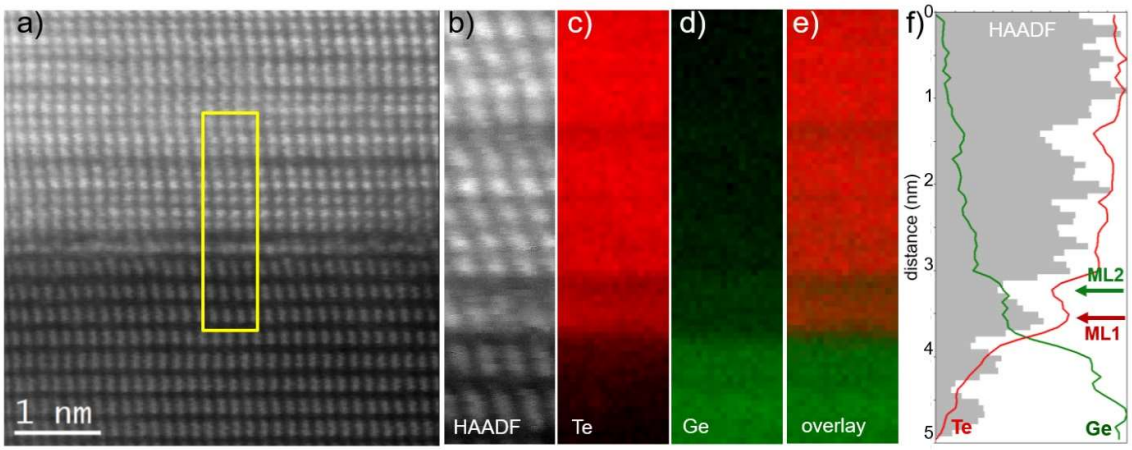

FIG. 3. (a) HAADF-STEM survey image showing the region of the EELS measurement. (b) HAADF-STEM signal acquired simultaneously with the EELS. (c,d) maps of the integrated Te $M_{4,5}$ and Ge $L_{2,3}$ EELS signals, (e) color overlay of (c), (d) and (f) plot of the integrated intensities of (b-d), showing the presence of Te in the bright ML1 (red arrow) and Ge in the darker ML (green arrow).

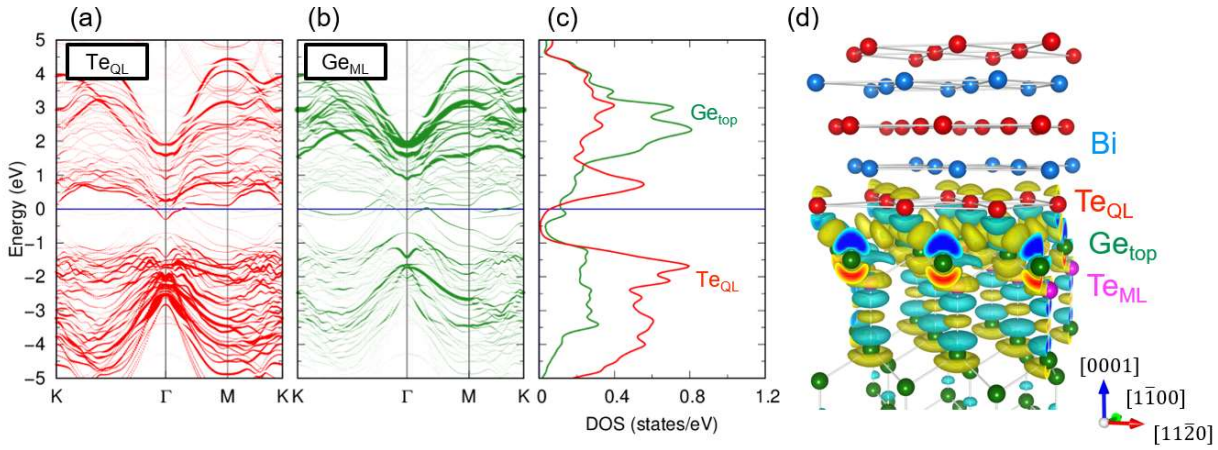

FIG. 4. Band structures and projections onto (a) Te_{QL}, and (b) Ge_{ML}, along the K → Γ → M → K direction in the 2D Brillouin zone. (c) Projected local DOS: Te_{QL} (red), Ge_{ML} (green). (d) Density change, $\Delta n = n_{Bi_2Te_3/Ge\text{-}Te/Ge(111)} - \left(n_{Bi_2Te_3/Ge} + n_{Ge\text{-}Te}\right)$, at the interface of Bi_2Te_3 (Bi: blue ball, Te: red), Ge-Te dumbbell (Ge: green, Te: magenta) and Ge substrate. (Isosurface = 0.001 e^-/a_B^3; maximum of the R-G-B color is 0.0025 e^-/a_B^3.)

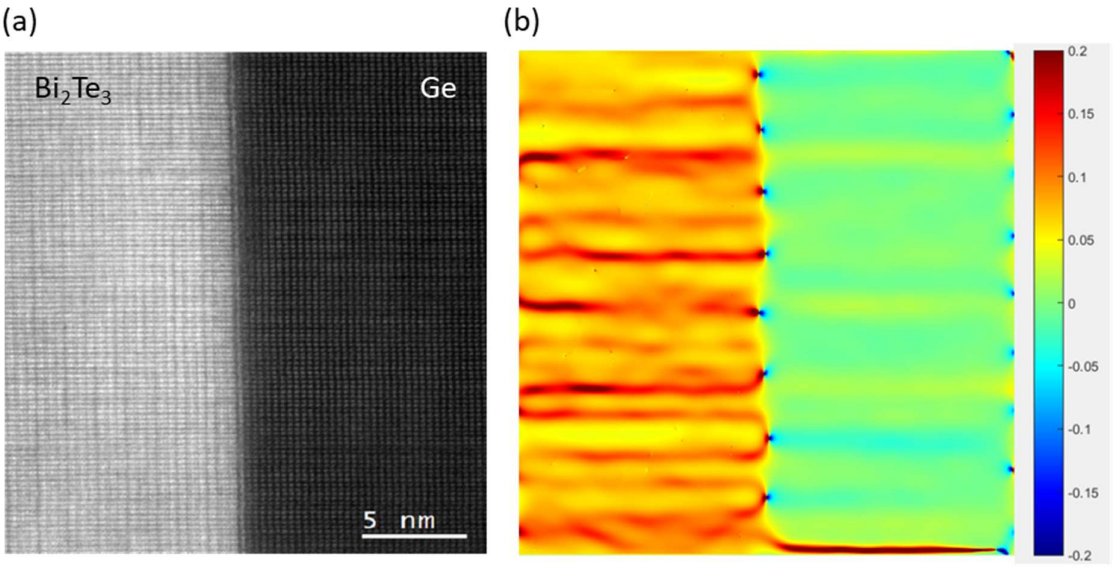

FIG. 5. (a) HAADF-STEM image of the area where the strain analysis was performed. (b) Strain map showing the locations of the interface misfit dislocation network due to strong bonding between the Bi_2Te_3 and Ge(111) substrate. The axes were chosen along the principal directions of elastic symmetry, taking the x-axis parallel to the interface and the y-axis normal to the interface.